AGU PUBLICATIONS

Water Resources Research

RESEARCH ARTICLE
10.1002/2016WR019983

Companion to *Vanderborght et al.* [2017] doi: 10.1002/2016WR019982.

Key Points:
- We evaluate different concepts to describe soil evaporation using numerical simulations
- Lateral transport in both soil and atmosphere determine local evaporation from heterogeneous surfaces
- Different parameterizations of vapor transport mainly affect diurnal dynamics of evaporation

Correspondence to:
J. Vanderborght,
j.vanderborght@fz-juelich.de

Citation:
Fetzer, T., J. Vanderborght, K. Mosthaf, K. M. Smits, and R. Helmig (2017), Heat and water transport in soils and across the soil-atmosphere interface: 2. Numerical analysis, *Water Resour. Res.*, *53*, 1080–1100, doi:10.1002/2016WR019983.

Received 20 OCT 2016
Accepted 5 DEC 2016
Published online 3 FEB 2017

Heat and water transport in soils and across the soil-atmosphere interface: 2. Numerical analysis

Thomas Fetzer [1], Jan Vanderborght [2,3], Klaus Mosthaf [4], Kathleen M. Smits [5], and Rainer Helmig [1]

[1]Institute for Modelling Hydraulic and Environmental Systems, Department of Hydromechanics and Modelling of Hydrosystems, University of Stuttgart, Stuttgart, Germany, [2]Agrosphere Institute, IBG-3, Forschungszentrum Jülich GmbH, Jülich, Germany, [3]Centre for High-Performance Scientific Computing in Terrestrial Systems, HPSC TerrSys, Geoverbund ABCJ, Forschungszentrum Jülich GmbH, Jülich, [4]DTU Environment, Technical University of Denmark, Kgs. Lyngby, Denmark, [5]Department of Civil and Environmental Engineering, Center for Experimental Study of Subsurface Environmental Processes, Colorado Schools of Mines, Golden, Colorado, USA

Abstract In an accompanying paper, we presented an overview of a wide variety of modeling concepts, varying in complexity, used to describe evaporation from soil. Using theoretical analyses, we explained the simplifications and parameterizations in the different approaches. In this paper, we numerically evaluate the consequences of these simplifications and parameterizations. Two sets of simulations were performed. The first set investigates lateral variations in vertical fluxes, which emerge from both homogeneous and heterogeneous porous media, and their importance to capturing evaporation behavior. When evaporation decreases from parts of the heterogeneous soil surface, lateral flow and transport processes in the free flow and in the porous medium generate feedbacks that enhance evaporation from wet surface areas. In the second set of simulations, we assume that the vertical fluxes do not vary considerably in the simulation domain and represent the system using one-dimensional models which also consider dynamic forcing of the evaporation process, for example, due to diurnal variations in net radiation. Simulated evaporation fluxes subjected to dynamic forcing differed considerably between model concepts depending on how vapor transport in the air phase and the interaction at the interface between the free flow and porous medium were represented or parameterized. However, simulated cumulative evaporation losses from initially wet soil profiles were very similar between model concepts and mainly controlled by the desorptivity, S_{evap}, of the porous medium, which depends mainly on the liquid flow properties of the porous medium.

1. Introduction

In an accompanying paper, Vanderborght et al. (P1), we presented an overview of different concepts and theories commonly used to describe evaporation from soil surfaces and derived simplifications of more comprehensive descriptions of the flow and transport processes. The main objective of this paper is to evaluate the consequences of model simplifications by performing exemplary simulations. The setup of these simulations is based on the outcome of P1 in which we identified three main groups of options for model simplifications. The first group deals with the dimensions of the process description (1-D versus 2/3-D) which depends on the decision to consider or neglect lateral fluxes and gradients in state. The second group is related to the description of vapor transport in the porous medium and the third group to the representation of the interaction between the porous medium and the free flow. The first set of simulations addresses option 1 and evaluates the effect of lateral variations in the porous medium properties and the coupling between lateral flow and transport processes in the porous medium and the free flow on evaporation processes. In the second set of simulations, to further investigate the effect of options 2 and 3, we assume a homogeneously evaporating surface and ignore any lateral variations thus representing the system in one-dimension. In these simulations, the exchange between the porous medium and the free flow is derived from the vertical gradients in state variables in the free flow using transfer resistances. Using this set of simulations, the effect of the representation of the vapor flow in the porous medium and the representation of the interaction between the porous medium and the free flow is evaluated. A simplified version of the 1-D model is then used to obtain (approximate)

Table 1. Parameters of the Mualem van Genuchten Hydraulic Functions [*van Genuchten*, 1980] for Two Different Soils

Texture	θ_r	θ_s	α (cm^{-1})	n	K_s ($cm\ d^{-1}$)	l
Silt	0.02	0.35	0.0042	1.324	91.2	0.5
Sandy loam	0.065	0.41	0.08	1.65	106.1	0.5

analytical expressions. We illustrate how these expressions can be used to evaluate model simplifications. Comparing simulation results, we then draw conclusions about the type of data or observations required to properly parameterize models of different complexity. This paper focusses on *qualitative* differences between modeling approaches to specifically address the question whether different model concepts lead to fundamental differences in fluxes dynamics that cannot be matched by changing the model parameters. A direct and *quantitative* comparison between simulation results and experimental observations, which also needs to address the parameterization problem, will be the focus of future work but is out of the scope of this paper.

2. Flow and Transport Properties of the Considered Porous Media

Two soil types were considered: a finer textured silt and a coarser textured sandy loam. The hydraulic properties are described by the Mualem van Genuchten functions [*van Genuchten*, 1980] and the parameters of the hydraulic functions are given in Table 1. To appraise the relevance of liquid and vapor fluxes for different soil water pressure heads, ψ (m), the hydraulic conductivity curves for the isothermal liquid $K_{l,\psi}$ ($m\ s^{-1}$) and vapor conductivity $K_{v,\psi}$ ($m\ s^{-1}$) at a temperature of 20°C and 40°C (only sandy loam soil) are shown in Figure 1. The relations of these conductivities to the fluid viscosity, (relative) permeability, the volumetric air phase content, and effective vapor diffusion coefficient in the porous medium, pressure head, relative air humidity, and temperature are given in equations (21) and (22) of P1. The effective vapor diffusion coefficient in the porous medium was described using the Millington Quirk equation [*Millington and Quirk*, 1961]. The conductivity curves illustrate that in the sandy loam soil, the vapor conductivity becomes more important than the liquid conductivity for pressure heads smaller than −30 m (≈−300 kPa) whereas for the silt soil, the liquid conductivity is more important for pressure heads larger than $-2{\cdot}10^3$ m (≈ −20 MPa). At 40°C, the liquid and vapor conductivities are, respectively, 1.5 and 3 times higher than at 20°C demonstrating the relative contribution of vapor transport at higher temperatures.

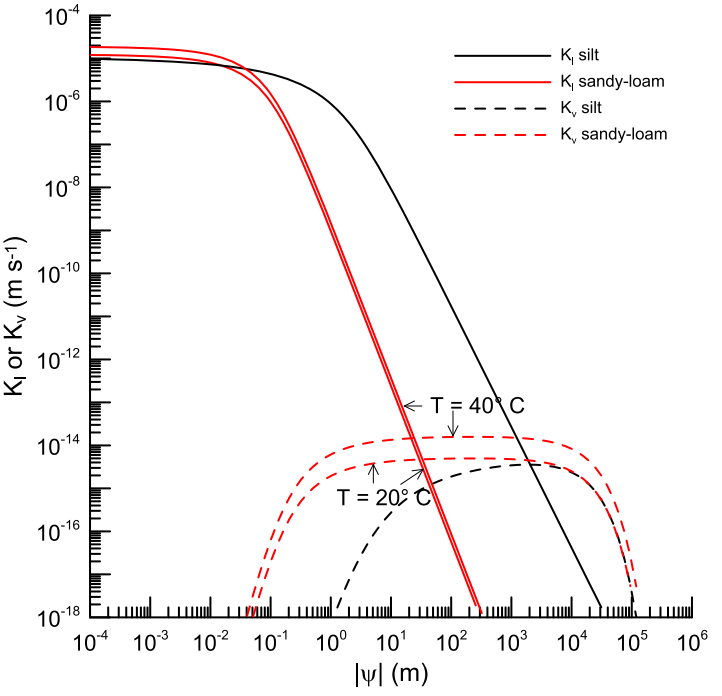

Figure 1. Isothermal hydraulic conductivity of the liquid ($K_{l,\psi}$ solid lines) and vapor phase ($K_{v,\psi}$ dashed lines) at 20°C as a function of the absolute value of the water pressure head, ψ, for the sandy loam and silty soil (see Table 1) and isothermal conditions. For the sandy loam soil, also conductivities at 40°C are shown.

3. Simulation Set 1: Effect of Lateral Transfer Processes

3.1. Model and Scenario Description

Simulations in the first set were performed using the two-phase two-component porous medium model that is coupled with the Reynolds-averaged Navier-Stokes (RANS) free flow model (fully coupled model).

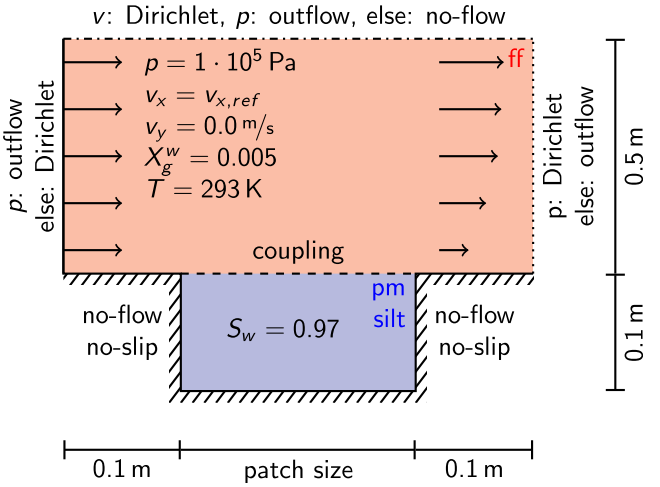

Figure 2. Setup for evaporation from a soil sample with different lengths/patch sizes: 0.1, 0.2, 0.5, 1.0, and 2.0 m. Air is flowing from left to right with different wind speeds $v_{x,ref}$: 0.5, 1.0, and 5.0 m s^{-1}. The discretization is equidistant in the horizontal direction (Δx=0.02 m), in the vertical direction 20 cells are located in the free flow and 10 in the porous medium, both with a grading toward the interface.

Simulations were carried out using the open-source simulator DuMu^x [*Flemisch et al.*, 2011; *Schwenck et al.*, 2015], which is based on the numerical toolbox DUNE [*Bastian et al.*, 2008a, 2008b]. The equations were discretized fully implicitly in time and using the box-method in space [*Baber et al.*, 2012; *Helmig and Huber*, 1998].

The scenarios varied the length of the domain (e.g., short versus long test sections) and lateral variations in the porous medium properties (e.g., homogeneous versus heterogeneous). Boundary conditions (wind speed, air temperature, and humidity of inflowing air) were kept constant in time. As demonstrated below, both variations led to lateral variations in state variables in the free flow, lateral fluxes in the porous medium, and lateral variations in the vertical fluxes at the porous medium-free flow interface.

3.2. Effect of Soil Sample Length and Wind Speed on Evaporation: Impact of Gradients in the Free Flow

In the first scenario, the effect of the length of a wet soil patch downstream of a uniform and constant dry air flow on the evaporation rate for different wind speeds (0.5–5 m s^{-1}) was simulated. Specifications of the simulation domain, discretization, initial, and boundary conditions are given in Figure 2.

As shown in Figure 3, the average evaporation rate from a wet patch clearly increased with decreasing patch size. In addition, the evaporation rate increased with increasing wind speeds and the relative increase of evaporation with decreasing patch size was similar for different wind speeds, except for the smallest patch sizes. The larger patches had lower evaporation than the small patches based on the changes in the free flow humidity. Because the air was more saturated with water vapor when it flows along the downstream section of the larger patch, the evaporation rate for the downstream section was lower, making the overall evaporation rate lower. This illustrates the effect of lateral variations in relative air humidity,

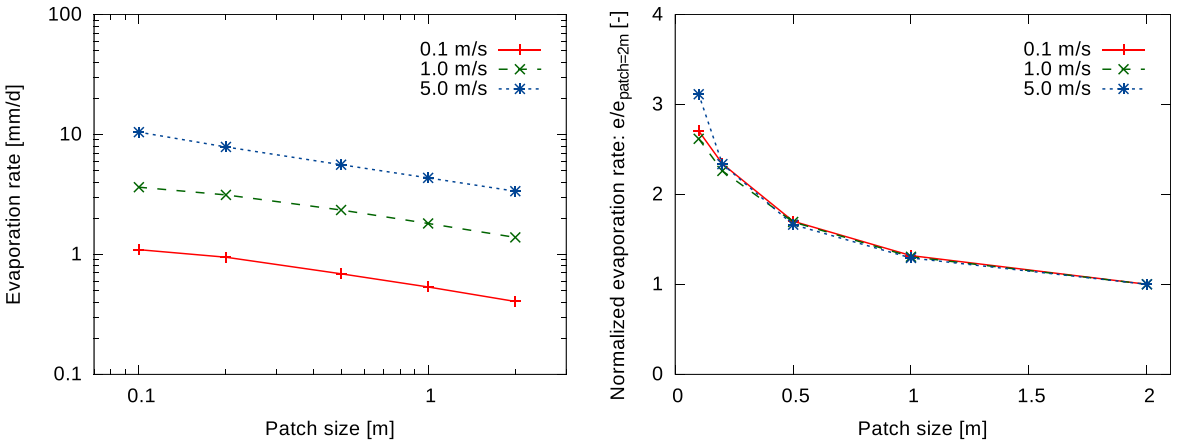

Figure 3. Simulated stage I steady state evaporation rates from wet silt soil patches with different patch sizes. The normalized evaporation rate is the evaporation rate divided by the evaporation rate obtained from the maximum patch size (2 m).

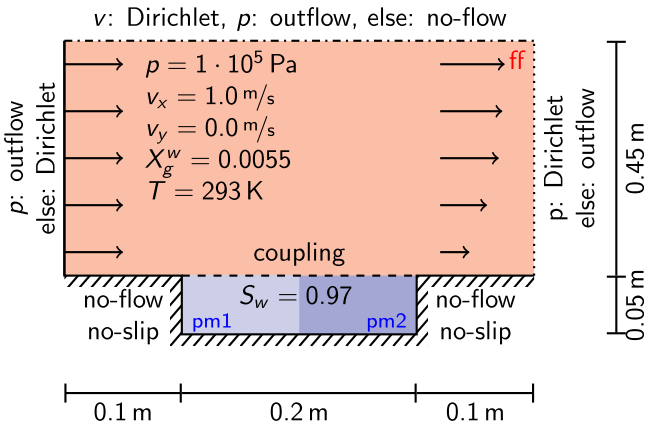

Figure 4. Setup for evaporation from a homogeneous/heterogeneous soil sample. In the homogeneous case, the porous medium is filled with silt, in the heterogeneous case one part is filled with silt and the other with sandy loam. Air is flowing from left to right, the porous medium is fully isolated. The problem discretized using 41 cells in horizontal and 40 cells in vertical direction (25 in the free flow and 15 in the porous medium) with a grading toward the interface.

temperature, and wind speed that emerge above an evaporating surface with finite length on the exchange process.

3.3. Effect of Soil Heterogeneity on Evaporation

To investigate the effect of soil type (i.e., silt and sandy loam) and orientation on evaporation, simulations were run in which two soil blocks were placed adjacent to each other as seen in Figure 4. In the first test case, the silt block was placed upstream (left) from the sandy loam block and vice versa for the second case. In a third case, a homogeneous silt block was considered. To evaluate the influence of lateral liquid and heat fluxes within the porous medium, we considered a fourth and a fifth set of simulations in which either lateral water or heat fluxes between the two blocks were blocked.

3.3.1. Impact of Heterogeneities in the Porous Medium

Figure 5 shows the evaporation rates from the homogeneous and heterogeneous test cases. For the homogeneous silt case, a steady state evaporation rate was obtained during the first day that remained constant until day 3 when the evaporation rate decreased. Feedbacks between free and porous-medium flow result in higher humidities as the air flows along the test section, the evaporation rate from the downstream half of the test section was smaller than from the upstream half. The evaporation rate from the upstream part decreased a little earlier than the downstream part, which led to a short peak in evaporation from the downstream part. Since the initial water distribution was uniform in the simulation domain, this illustrates that lateral water flow in the porous medium compensated for the higher evaporation losses in the upstream part. Lateral variations in air humidity and temperature in the free flow, which led to lateral variations in evaporation rate, also induced lateral liquid flow in the porous medium. These lateral fluxes effectively homogenized the effect of spatial variations of fluxes at the porous medium surface so that the homogeneous porous medium could have been represented by a 1-D vertical profile.

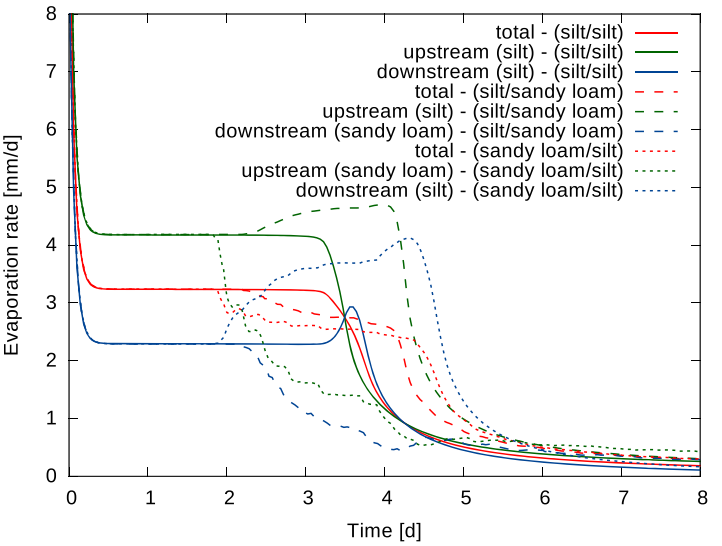

Figure 5. Evaporation rates from a homogeneous soil and a soil with a heterogeneity in the horizontal direction (see Figure 4). Red lines represent average evaporation rates from the entire simulation domain, green lines from the upstream part, and blue lines from the downstream. Full lines are evaporation rates for the homogeneous case (both parts are filled with silt), dashed lines for the case that the upstream part is filled with silt and the downstream part with sandy loam, and dotted lines for the upstream part filled with sandy loam and the downstream part with silt.

In the heterogeneous test cases (i.e., silt and sandy loam, see Figure 4), the evaporation rates from both the silt and sandy loam were initially the same. When the water content at the soil surface is sufficiently high, the vapor pressure at the soil

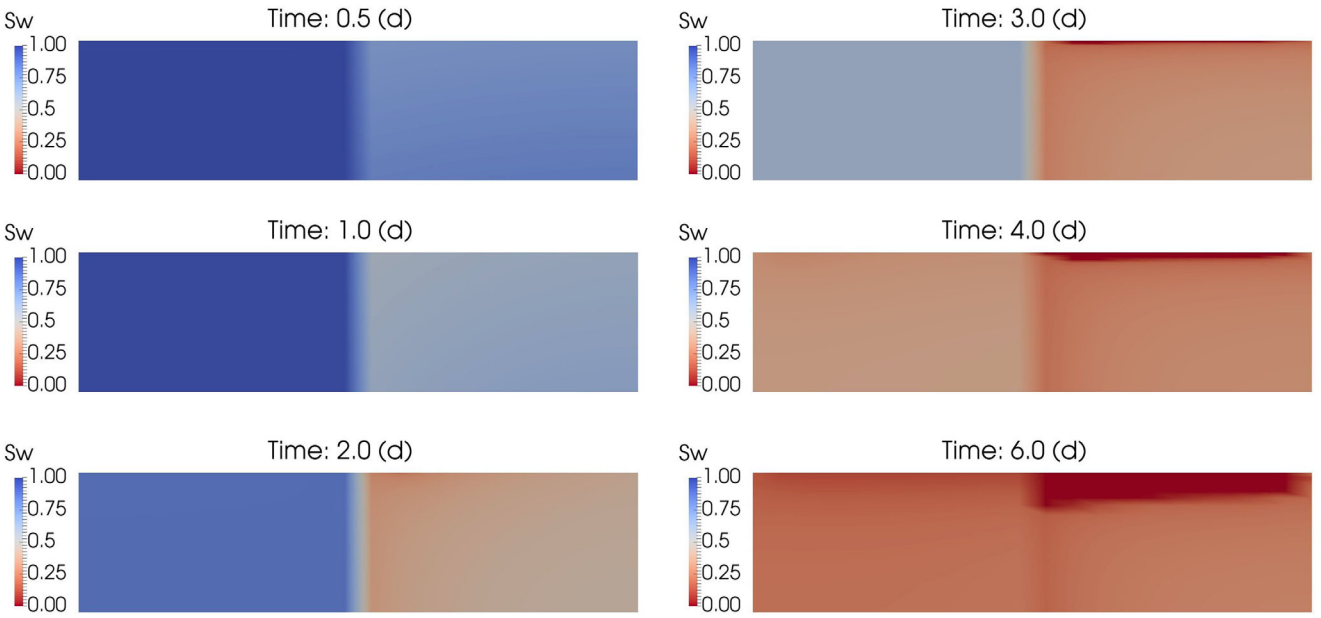

Figure 6. Drying process for a heterogeneous porous medium over time (see Figure 4 for setup). The water saturation (S_w) distribution in the porous medium is shown at six different times. The left/upstream half of the domain is silt, the right/downstream half is sandy loam.

surface is close to the saturated vapor pressure and the evaporation is controlled by the atmospheric conditions and the surface roughness, oftentimes referred to as stage I evaporation, but not by the porous medium hydraulic properties. However, the sandy loam section's evaporation rate started to decrease earlier than evaporation from the finer silty part, related to the differences in soil hydraulic properties. This falling rate period correlates to the soil entering into stage II evaporation.

The decrease in evaporation from the sandy loam part occurred in two steps in this example. The first gradual decrease occurred as the surface of the sandy loam was dried out and the residual water content was reached (Figure 6). During this time, the finer silt material continued to evaporate at a high rate and did not dry out. The silt material functioned as a wick that drained water from the adjacent sandy loam resulting in a longer sustained high evaporation from the silt material than in the homogeneous silty test case. This behavior was also demonstrated in lab experiments [*Lehmann and Or*, 2009]. The decrease in evaporation from the sandy loam was accompanied by an increase in evaporation from the silt part.

The second smaller decrease in evaporation rate from the sandy loam occurred when the liquid water flow to the evaporation front in the sandy loam soil driven by gradients in capillary forces was reduced by the limited water supply due to the no-flow bottom boundary condition of the box. With a deeper porous-medium box, the decrease would be continuous. After the second decrease of evaporation from the sandy loam, also the silt started drying out. Also the second drop in evaporation rate from the sandy loam surface corresponded with a further increase in evaporation rate from the silt surface, despite the drying of the silt surface. This shows that for a heterogeneous surface, the evaporation rate may locally increase and become even larger than from a homogeneous surface. The increase in evaporation from the silt part was larger when it was located downstream of the sandy loam part. In this case, the temperature and humidity of the air that flowed over the silt part, respectively, increased and decreased when the evaporation from the upwind part decreased.

When the finer silt part was upstream of the sandy loam, the evaporation rate from the silt also increased when evaporation from the sandy loam part decreased. This indicates that, in this case, lateral mixing in the air increased temperature and reduced humidity in the upwind direction above the silt part. Another potential reason is the lateral heat flux in the porous medium, which increases the temperature at the surface of the silt soil when evaporation from the sandy loam part changed.

Table 2. Average Vapor Concentration, ρ_g^w, Temperature, T, and Evaporation Flux, F_w, at the Surface of the Upstream and Downstream Part of the Homogeneous/Heterogeneous Porous Medium After 3 Days of Evaporation (Figure 5), 1-D Aerodynamic Resistances, r_V, for the Upstream and Downstream Parts That are Derived From Evaporation Rates and Vapor Concentrations in the Homogeneous Setup After 3 Days of Evaporation, and Calculated Fluxes Using the 1-D Aerodynamic Resistances, r_V

	Upstream Part	Downstream Part	Inflow
	Slit	Slit	
$\bar{\rho}_g^w$ (kg m^{-3})	9.33 10^{-3}	9.12 10^{-3}	6.52 10^{-3}
T (K)	283.12	282.73	293
$\bar{F}_w$ (FC)[a] (kg m^{-2} s^{-1})	4.81 10^{-5}	2.64 10^{-5}	
r_V (s m^{-1})	58.4	98.5	
	Silt	Sand	
$\bar{\rho}_g^w$ (kg m^{-3})	9.56 10^{-3}	8.45 10^{-3}	
T (K)	283.43	284.32	
$\bar{F}_w$ (FC) (kg m^{-2} s^{-1})	5.28 10^{-5}	1.27 10^{-5}	
$\bar{F}_w$ (1-D) (kg m^{-2} s^{-1})	5.20 10^{-5}	1.96 10^{-5}	
	Sand	Silt	
$\bar{\rho}_g^w$ (kg m^{-3})	7.62 10^{-3}	9.64 10^{-3}	
T (K)	286.97	283.55	
$\bar{F}_w$ (FC) (kg m^{-2} s^{-1})	1.87 10^{-5}	4.16 10^{-5}	
$\bar{F}_w$ (1-D) (kg m^{-2} s^{-1})	1.88 10^{-5}	3.17 10^{-5}	
$\bar{F}_w$ (1-D) (kg m^{-2} s^{-1})[b]		5.34 10^{-5}	

[a]FC = fully coupled model.
[b]The aerodynamic resistance of the upstream part is used to calculate the evaporation from the downstream part. It is assumed that the mass transfer boundary layer is equal to the one above the upstream part when the upstream part does not evaporate anymore.

3.3.2. Impact of Changing Lateral Gradients in the Free Flow Above Drying Heterogeneous Porous Media

To evaluate the influence of changes in lateral gradients in the free flow above a drying heterogeneous porous medium on the evaporation, we derived in a first step 1-D aerodynamic resistances (Table 2), r_V (s m^{-1}) for the upstream and downstream part of the homogeneous porous medium using:

$$r_V = \frac{\bar{\rho}_g^w(z=0) - \rho_{g,inflow}^w}{\bar{F}_w} \tag{1}$$

where and $\rho_{g,inflow}^w$ (kg m^{-3}) is the vapor concentration in the inflowing air, $\bar{\rho}_g^w(z=0)$ the average vapor concentration at the interface in the up or downstream part and $\bar{F}_w$ (kg m^{-2} s^{-1}) the average vapor flux from the up or downstream part. The vapor concentrations and fluxes during stage I evaporation were used to calculate the r_V's. These r_V's were subsequently used to calculate the evaporation rates from the heterogeneous porous medium using the vapor concentrations in the inflowing air and at the soil surface of the up and downstream parts when evaporation of one of the parts ceased (Table 2), which influenced the lateral gradients in air humidity and temperature.

For the upstream part, the evaporation rates were fairly well reproduced using the 1-D aerodynamic resistances (see Table 2). This indicates that the air humidity and air temperature profiles in the upstream part are mainly defined by the vapor concentration and temperature at the porous medium surface and in the inflowing air. The increase in evaporation rate from the upstream silt part when the evaporation from the downstream sandy loam part ceased could be linked to an increase in vapor concentration and temperature at the porous medium surface. Whether this increase in surface temperature and vapor concentration can be predicted based on the lateral heat transfer in the porous medium alone still needs to be investigated. When the dry and less-evaporating sandy loam part was upstream, its lower evaporation rate could also be reproduced fairly well from the surface vapor concentration and the 1-D aerodynamic resistance.

The conditions in the free flow in the downstream part, that being vertical profiles of air humidity and temperature, were strongly influenced by evaporation from the upstream part and changed when the evaporation from this part changed. These temporal changes in air humidity profiles due to changing evaporation rates in upstream parts from heterogeneous surfaces could not be represented by 1-D aerodynamic resistances that were derived for other evaporation conditions in the upstream part.

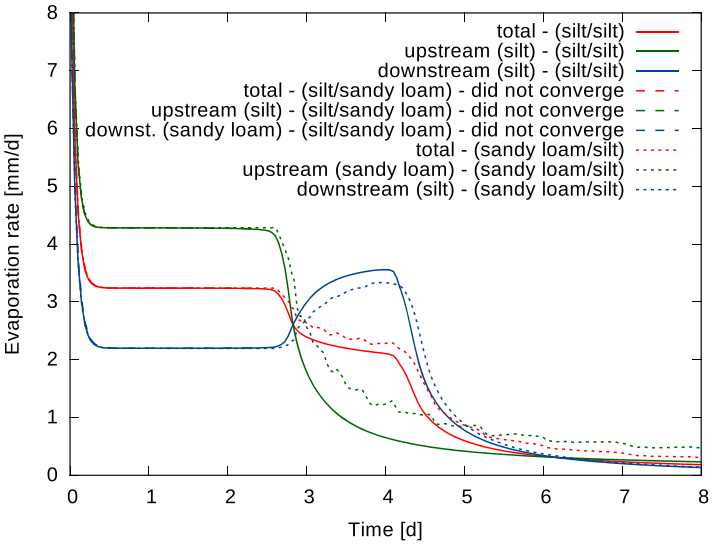

Figure 7. Evaporation rates for the same setup as shown in Figure 4 and Figure 5 but for the case that exchange of heat and water across the vertical interface between the upstream and downstream parts of the domain were disabled.

3.3.3. Impact of Lateral Water and Heat Fluxes in the Porous Medium

Figure 7 shows simulated evaporation rates for the case that lateral water flow and conductive heat transfer between up- and downstream parts are blocked. For the homogeneous setup, blocking of lateral transfer between the up and downstream parts led in the upstream part to an earlier transition to stage II evaporation compared with the case in which lateral transfer between the two parts could take place (cf., Figure 5 and Figure 7). The decrease in evaporation from the upstream part led to a lower air humidity above the downstream part and an increase in evaporation from the downstream part. For the heterogeneous setups, the switch to stage II evaporation occurred earlier in the silty material, which could not rely on liquid water transfer from the sandy loam, and later in the sandy loam material, compared to the cases where lateral water transfer between the two parts could take place.

In Figure 8, simulated evaporation rates are shown for the case that conductive heat transfer between up and downstream parts are blocked but lateral water flow is allowed. These simulation results show more similarities with the simulation results including full lateral transfer (cf., Figure 5 and Figure 8). However, the increase in evaporation from the silt part at the time when the evaporation from the sandy loam part decreased was clearly less than for the case also lateral conductive heat fluxes in the porous medium were considered. This is especially clear when the silt part is located upstream of the sandy loam part. When conductive heat transfer between the silt and sandy loam blocks was blocked, the evaporation rate in the upstream silt block did not increase when the evaporation from the downstream sandy loam part decreased (Figure 8) and its temperature increased. This demonstrates that the increase in evaporation from the upstream silt part when the evaporation from the downstream sandy loam part decreased and that was simulated with full lateral transfer (Figure 5) was due to conductive heat fluxes in the porous medium rather than heat transfer through the air flow.

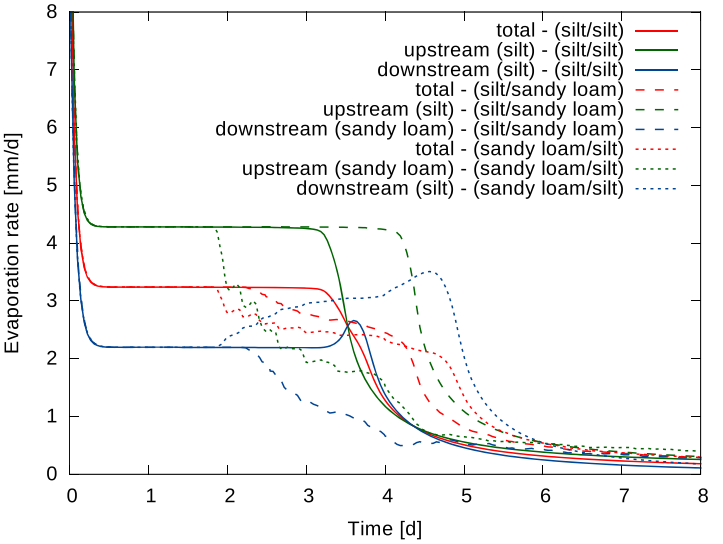

Figure 8. Evaporation rates for the same setup as shown in Figures 4 and 5 but for the case that conductive heat fluxes across the vertical interface between the upstream and downstream parts of the domain were disabled.

4. Simulation Set 2: Dynamic Forcing of Evaporation

4.1. Used Models and Considered Simulations

In this example, the effect of different model concepts on simulated evaporation from a

homogeneous surface under dynamic forcing is investigated. In contrast to the previous examples, lateral variations in state variables and in vertical fluxes at the porous medium-free flow interface were assumed to be negligible so that the flow and transport process in the porous medium could be represented as a 1-D process. The transfer or fluxes of water and heat between the porous medium and the free flow could be described using transfer resistances, vapor concentrations, and temperatures at the porous medium-free flow interface and at a reference height in the free flow (equation (1)). The transfer resistances depend on the wind profile, which for a homogeneous surface can be represented by a logarithmic profile, and on the roughness of the surface (see equations (50), (51), (57), and (58) in P1). The fluxes between the porous medium and the free flow were then used as boundary conditions to solve the water and heat balance equations in the porous medium. Furthermore, vertical gas phase fluxes in the porous medium were neglected so as the transport of the dry air component. The most comprehensive model for this simulation set was the one component (water) one-and-a-half phase (liquid phase and only diffusion in the gas phase) model (for details see P1) that is coupled with the heat flow equation. We will call this model also the nonisothermal vapor-water flow model.

Simulations by this model were compared to simulations with the Richards equation which only considers isothermal flow and transport of the component water in the liquid phase (isothermal, one component, one phase) that is decoupled from the heat flux in the porous medium. For a sufficiently wet soil surface when the vapor concentration is close to the saturated vapor concentration, the coupling of the Richards equation with the heat fluxes is done at the free-flow porous medium interface where a surface energy balance is solved to determine the potential evaporation flux across the surface, that is, the stage I evaporation rate. This potential evaporation rate was used as a flux boundary condition for the Richards equation. This surface heat balance uses the same transfer resistances for vapor and sensible heat transfer in the free flow as the one component one-and-a-half phase model but assumes that vapor concentration at the surface is always saturated. The reduction of evaporation during stage II evaporation, when the soil surface dries out and the surface vapor concentration is significantly lower than the saturated one, was represented using a threshold formulation of the boundary condition. The flux boundary condition was switched to a constant pressure head boundary condition when the water pressure head at the soil surface reached a critical value, ψ_{crit}. Since the pressure head is kept fixed and independent of other boundary conditions in this model during stage II evaporation, the water fluxes from the deeper soil to the soil surface and the evaporation rate are decoupled from the evaporative forcing (radiation, wind speed, air humidity, and temperature). The sensitivity of the simulation results to the choice of ψ_{crit} in soils with different hydraulic properties was evaluated by using an analytical approximation of the Richards equation. This analytical approximation was furthermore used to evaluate the impact of vapor transport under isothermal conditions.

An alternative to the threshold boundary condition formulation for the Richards equation is to include a term in the transfer resistance that represents the resistance to vapor transfer from the evaporation surface toward the soil surface. This resistance is accounted for by multiplying the potential evaporation by a β-factor (see equation (60) P1) that is a function of the water content of the soil surface. In this model, the evaporation rate during stage II, that is, when $\beta < 1$, is still coupled to the evaporative forcing through the potential evaporation rate. Therefore, this can be considered to be a semicoupled description. We evaluated how this parameterization depends on the choice of the thickness of the surface layer and on other parameters such as the surface temperature using simulations with the nonisothermal vapor-water flow model.

In order to evaluate the sensitivity of the simulation results to vapor transport and processes that influence the parameterization of this transport (e.g., local thermal nonequilibrium effects which are represented by an enhancement η of the thermal hydraulic conductivity for vapor transport, K_{vT} ($m^2\ K^{-1}\ s^{-1}$) (see equation (24) of P1), or turbulent pumping which can be represented by a higher vapor diffusion coefficient), simulations were performed for different sets of parameterizations.

4.2. Boundary Conditions and Simulation Setup

The forcing boundary conditions at the soil surface represent an 11 day period in August 2010 at the Selhausen test-site (50° 52′ 47.89″ N, 6° 26′ 33.14″ E) close to Jülich (Germany). Radiation, wind speed, relative humidity, and air temperature measured at 2 m height were assumed to be representative of the entire field (Figure 9). A flat bare soil surface with a roughness height, d, of 2 mm was assumed. The surface albedo was 0.23 and the thermal emissivity of the soil surface was set to 0.9. A soil profile with a depth of 1 m was

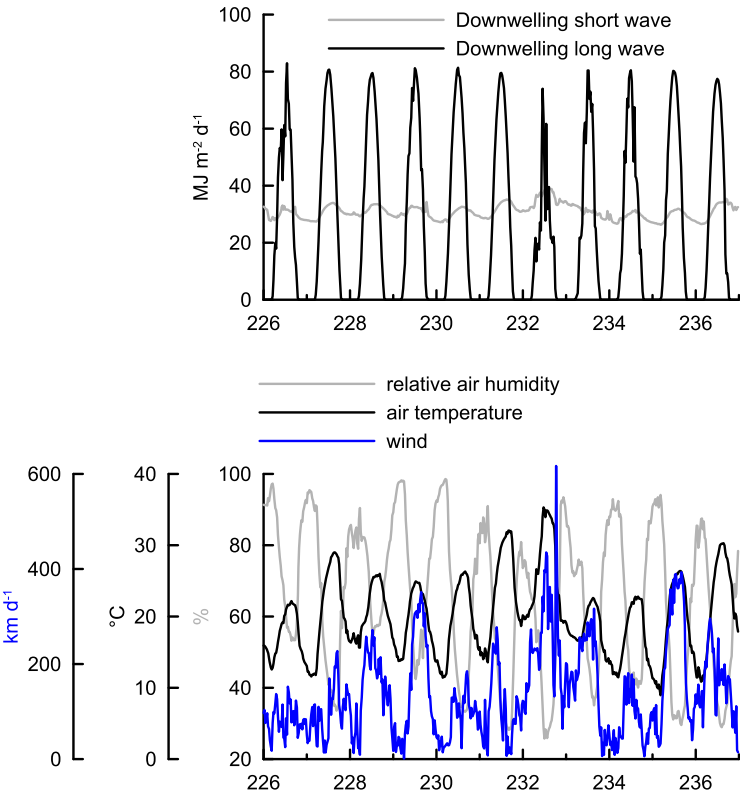

Figure 9. (top) Time series of downwelling short and longwave radiation and (bottom) wind speed, air temperature, and air humidity at 1.45 m height.

considered and at the bottom of the soil profile, a constant temperature (15°C) and zero pressure gradient in the liquid phase was assumed. The initial conditions in the two soil profiles with different soil hydraulic properties were defined so that the initial volumetric water content in the profiles was similar, that is, $\theta \approx 0.2$. Simulations were carried out using Hydrus 1-D [*Saito et al.*, 2006; *Simunek et al.*, 2008; *Šimůnek et al.*, 2016] which was slightly changed so that downwelling long wave radiation, surface roughness, and enhancement factors η could be defined by the user.

4.3. Effect of Assuming Isothermal Processes Under Dynamic Forced Evaporation

The potential evaporation rates and simulated evaporation rates from the two soils using the nonisothermal vapor-water flow model (one component, one-and-a-half phase) and the Richards equation with two different boundary condition thresholds: $\psi_{crit} = -10^4$ cm or $\psi_{crit} = -10^5$ cm are shown in Figure 10. For the same test cases, simulated pressure heads at the soil surface and cumulative evaporation losses are given in Figures 11 and 12, respectively. As expected, for both soils, the simulated evaporation rate of the drying soil surface became smaller than the potential evaporation rate after a certain time (Figure 10). The simulated evaporation rate and cumulative evaporation losses were larger in the silt than in the sandy loam soil (Figure 12).

For the Richards equation models, the evaporation rate became smaller than the potential evaporation rate when the threshold pressure head at the surface was reached (stage II). In the nonisothermal vapor-water flow model, this happened due to a simulated decrease in air humidity at the soil surface when the soil surface dried out. For the sandy loam soil, the difference in the simulated evaporation rate and cumulative evaporation losses for the two different threshold pressures is hardly noticeable, whereas for the silt soil, the evaporation rates and cumulated evaporation are noticeably smaller for the larger ψ_{crit}.

In the silt soil, the diurnal temporal dynamics of the evaporation rate that was simulated using the nonisothermal vapor-water flow model was well reproduced by the Richards equation. During the morning hours, the actual evaporation rate kept up with the potential evaporation until the soil surface dried out and the evaporative demand could not be maintained by upward flow from deeper in the soil profile. From that moment on, the actual evaporation rate decreased with time and decoupled from the diurnal dynamics of radiation, air temperature, and relative air humidity. During the late afternoon or evening, the decreasing radiation and air temperature and increasing air humidity led to a drop in evaporative demand by the atmosphere and the evaporative demand could again be supplied by water fluxes from the soil profile. The lower evaporative demand led to a relaxation of the pressure heads at the soil surface.

During night, the soil surface layer was replenished by upward water flow from the deeper soil. In the silt soil during night and a considerable part of the day, the pressure heads at the soil surface were larger than

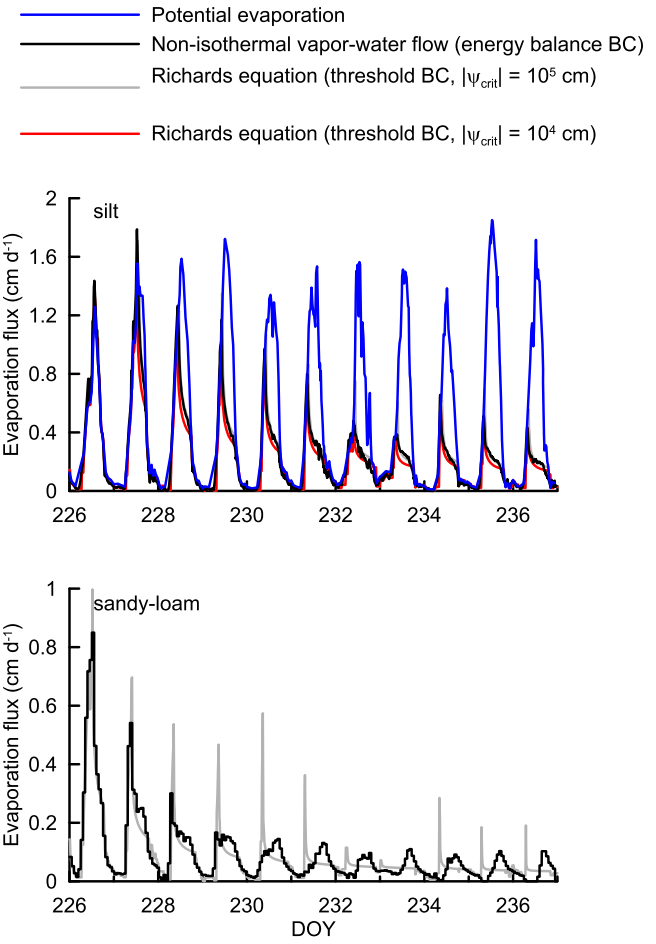

Figure 10. Time series of simulated evaporation rate from the (top) silt soil and (bottom) sandy loam soil using a model that considers nonisothermal vapor-water flow (black line) and using the Richards equation with threshold boundary conditions for $\psi_{crit} = -10^4$ cm (red line) or $\psi_{crit} = -10^5$ cm (grey line). The blue line represents the potential evaporation rate from a wet soil surface. Note the different scale of the *y* axes for the two plots. For the sandy loam, simulated evaporation using Richards equation overlapped for the two boundary thresholds.

$-2{\cdot}10^5$ cm (Figure 11), that is, the pressure head below which vapor conductivity, $K_{v,\psi}$, becomes larger than liquid conductivity, $K_{l,\psi}$, (Figure 1) so that evaporation dynamics were closely linked to liquid water fluxes. This explains why the Richards and the nonisothermal water vapor flow model simulate similar evaporation dynamics for this soil.

In the sandy loam soil, the diurnal dynamics of the evaporation and the pressure heads during night simulated by the nonisothermal water vapor flow model started deviating between the different models after 3 days (from DOY 229). From this day, the simulated pressure heads at the soil surface became significantly smaller than $-3{\cdot}10^3$ cm, that is, the pressure head below which $K_{v,\psi} > K_{l,\psi}$, during the whole day. The diurnal dynamics of evaporation from the soil surface was therefore controlled by vapor transport in the surface soil layer and seemed to be coupled again with the diurnal forcing. When the soil surface is dry, the gradient in water content that drives diffusive water flow cannot increase during the day. During the day the dry soil surface heats up, leading to downward directed thermal gradients so that the water/vapor flow that is driven by a thermal gradient reduces the evaporation rate during the day. The increase in evaporation during the day must therefore be due to an increase with temperature of the isothermal hydraulic conductivity for liquid, $K_{l,\psi}$, and mainly for vapor transport, $K_{v,\psi}$ (see Figure 1). It is evident that these dynamics cannot be reproduced by an isothermal Richards equation based model with a fixed pressure head at the soil surface.

4.4. Analytical Approximations of the Richards Equation to Assess the Influence of Vapor Transport on Cumulative Evaporation and to Determine ψ_{crit}

Despite the fact that the diurnal dynamics of the evaporation rate in the sandy loam soil were not well reproduced by the Richards equation, the simulated cumulative evaporation rates by the nonisothermal vapor liquid model and Richards equation were still in relatively close agreement (Figure 12), as was also concluded by *Assouline et al.* [2013] and *Milly* [1984]. This suggests that the cumulative evaporative water losses are controlled mainly by the transfer of liquid water from the deeper soil toward the evaporative front rather than by diffusive vapor transfer from the evaporative front toward the soil surface. The diurnal dynamics of the evaporation process, however, are controlled by temperature dependent vapor transfer from the evaporative front during the day, leading to a drying of the soil surface layer and rewetting of this layer during night by liquid water flow and vapor condensation [*Assouline et al.*, 2013].

An inspection of the θ-based formulation of the isothermal, one-component, one-and-a-half phase equation:

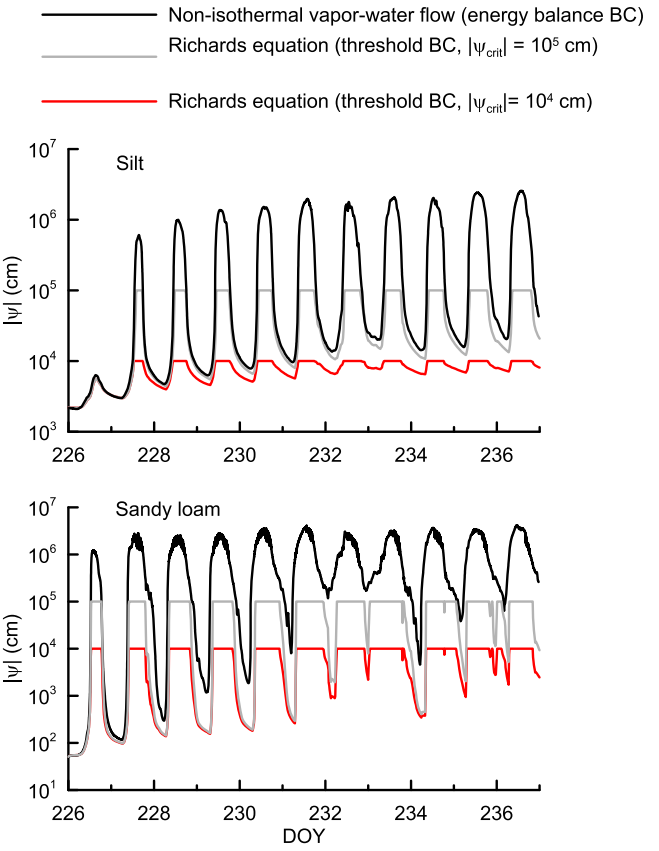

Figure 11. Evolution of the absolute pressure head, $|\psi|$, that is simulated at the (top) soil surface of the silt soil and (bottom) sandy loam soil using a nonisothermal vapor-water flow model (black line) and Richards model with a threshold boundary condition for $\psi_{crit} = -10^4$ cm (red line) or for $\psi_{crit} = -10^5$ cm (grey line).

$$\frac{\partial\theta}{\partial t} = \frac{\partial}{\partial z}\left(D_w(\theta)\frac{\partial\theta}{\partial z}\right) + \frac{\partial K(\theta)}{\partial z} \quad (2)$$

where $\theta = \theta_l + \theta_v$ is the sum of the liquid and vapor water content both expressed as volume liquid water per bulk volume of soil and water diffusivity D_w ($m^2\ s^{-1}$) is:

$$D_w = \left(K_{l,\psi} + K_{v,\psi}\right)\frac{\partial\psi}{\partial\theta} \quad (3)$$

(see equation (25) in P1) can be used to explain the similar cumulative evaporation losses that were simulated by the Richards equation and by the nonisothermal vapor-water flow model. It allows furthermore (i) evaluating the relative importance of liquid water flow toward an evaporating surface compared with vapor transport from the evaporating surface toward the soil-atmosphere interface and (ii) determining a suitable value of the threshold boundary condition ψ_{crit} for the Richards equation. When flow due to gravity (second term of the right hand side of equation (2)) can be neglected, equation (2) can be reduced to an ordinary differential equation using the Boltzmann transform $\lambda = \frac{|z|}{\sqrt{t}}$:

$$-\frac{\lambda}{2}\frac{d\theta}{d\lambda} = \frac{d}{d\lambda}\left(D_w\frac{d\theta}{d\lambda}\right) \quad (4)$$

For the case of a uniform initial water content, θ_i, which corresponds with $\theta(\lambda=\infty)$, and an instantaneous reduction of the water content at the soil surface that remains constant over time, θ_{sur}, which corresponds with $\theta(\lambda=0)$, the solution of equation (4) leads to a unique $\theta(\lambda)$ profile. Figure 13 shows that soil moisture profiles simulated by the nonisothermal vapor-water flow fall nearly on one reference curve when plotted versus the rescaled depth λ. The area between this reference curve and the horizontal line that corresponds with θ_i, defines the desorptivity S_{evap} ($m\ s^{-0.5}$):

$$S_{evap} = \int_{\theta_{sur}}^{\theta_i}\lambda(\theta)d\theta = \int_0^{\infty}[\theta_i - \theta(\lambda)]d\lambda \quad (5)$$

From a water balance follows directly that the cumulative evaporation, E_{cum} (m), from a soil of which the soil surface moisture content is instantaneously reduced to a surface water content, θ_{sur}, that remains constant over time can be described as:

$$E_{cum} = S_{evap}\sqrt{t} \quad (6)$$

An instantaneous reduction of the surface water content to a fixed value θ_{sur} is not a realistic boundary condition. The 'Time Compression Analysis' (TCA) can be used to fix this problem. In TCA, the evaporation process is split in two periods: stage I between $t = 0$ and $t = t_c$ and stage II $t > t_c$. For stage II, the cumulative evaporation is described using the following adapted form of equation (6):

$$E_{cum} = S_{evap}\sqrt{t - t_c + t_p} \tag{7}$$

where t_p is the time that would be needed to evaporate the same amount of water when the surface water content is instantaneously dropped to θ_{sur} as during stage I. Similar forms of this model have been introduced by *Black et al.* [1969], *Boesten and Stroosnijder* [1986], and *Ritchie* [1972]. Figure 12 shows that cumulative evaporation losses can be reproduced relatively well by this simple model. The crucial parameter in this model is S_{evap} which is related to the water diffusivity as [*Parlange et al.*, 1985]:

$$S_{evap}^2 = \frac{8}{3}(\theta_i - \theta_{sur})^2 \int_0^1 (1-\Theta) D_w(\Theta) d\Theta \quad \Theta = \frac{\theta - \theta_{sur}}{\theta_i - \theta_{sur}} \tag{8}$$

$$S_{evap}^2 = \frac{8}{3}\int_{\psi sur}^{\psi i} (\theta_i - \theta(\psi))\left(K_{l,\psi}(\psi) + K_{v,\psi}(\psi)\right) d\psi \tag{9}$$

From equation (8) follows that the $S_{evap}{}^2$ is an integrated or weighted average diffusivity or conductivity over the range of soil water contents or pressure heads between the soil surface and water content or pressure head deeper in the soil profile. The effect of vapor transport on S_{evap} can be evaluated by calculating S_{evap} for $K_{v,\psi} = 0$ whereas the effect of the threshold pressure head ψ_{crit} can be inferred from calculating S_{evap} for $\psi_{sur} = \psi_{crit}$. In Table 3, S_{evap} calculated using equation (8) for the two different soils are given together with S_{evap} derived from fitting equation (7) to simulated cumulative evaporation (Figure 12). Also included in Table 3 is the cumulative evaporation during stage II evaporation, E_{cum}, that was simulated by the nonisothermal vapor-water flow model and by the Richards equation for two different ψ_{crit}. The calculated S_{evap} indicate that vapor transport had almost no effect on the cumulative evaporation in the silt soil whereas in the sandy loam soil there was a noticeable effect as was confirmed by the E_{cum} simulations. However, the effect of thermal gradients is not considered in S_{evap} so that a perfect correlation between S_{evap} and E_{cum} cannot be expected.

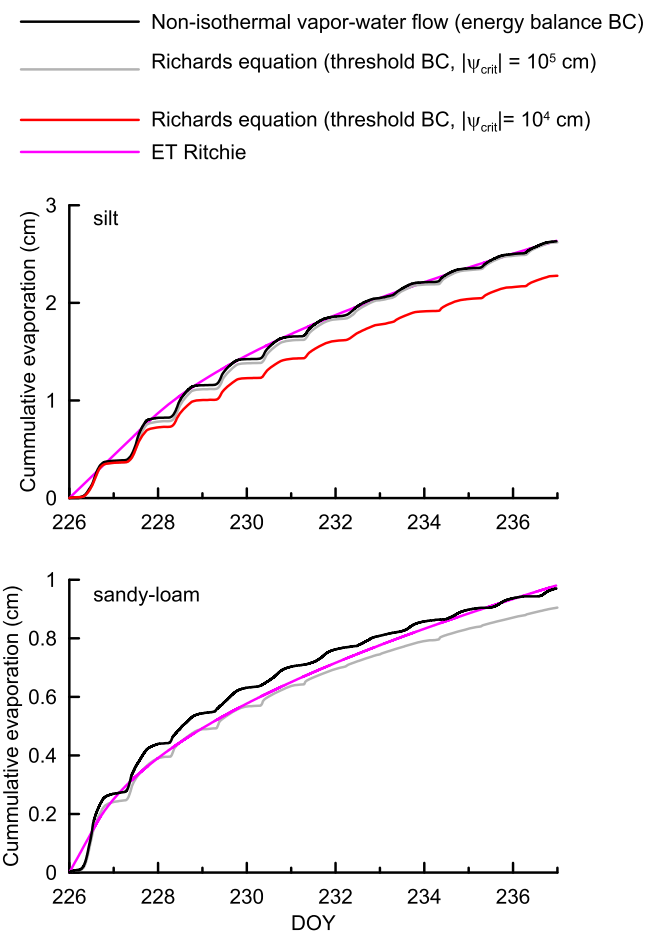

Figure 12. Cumulative evaporation in the (top) silt soil and (bottom) sandy loam soil simulated using the nonisothermal vapor-water flow model (black), the Richards model (equation (7)) with a threshold boundary condition $\psi_{crit} = -10^4$ cm (red line) or $\psi_{crit} = -10^5$ cm (grey line), and the Ritchie model (magenta). The cumulative potential evaporation for the considered period was 5.24 cm.

For the boundary conditions that we considered, the downward directed thermal gradients led to a smaller increase in E_{cum} when using the nonisothermal vapor-water flow model compared to simulations with the Richards equation than expected from the increase of S_{evap} from including vapor transport through $K_{v,\psi}$. Also the effect on the simulated cumulative evaporation of the threshold ψ_{crit} in the two different soils can be evaluated using S_{evap}. For the sandy loam soil, there was no difference in S_{evap} and E_{cum} for $\psi_{crit} = -10^4$ or -10^5 cm whereas S_{evap} and E_{cum} for the silt soil were clearly smaller for $\psi_{crit} = -10^4$ cm than for $\psi_{crit} = -10^5$ cm. This indicates that S_{evap} can be used as an indicator to demonstrate the relevance and importance of vapor flow and to define a suitable critical surface pressure head for a threshold boundary condition. S_{evap} also indicates

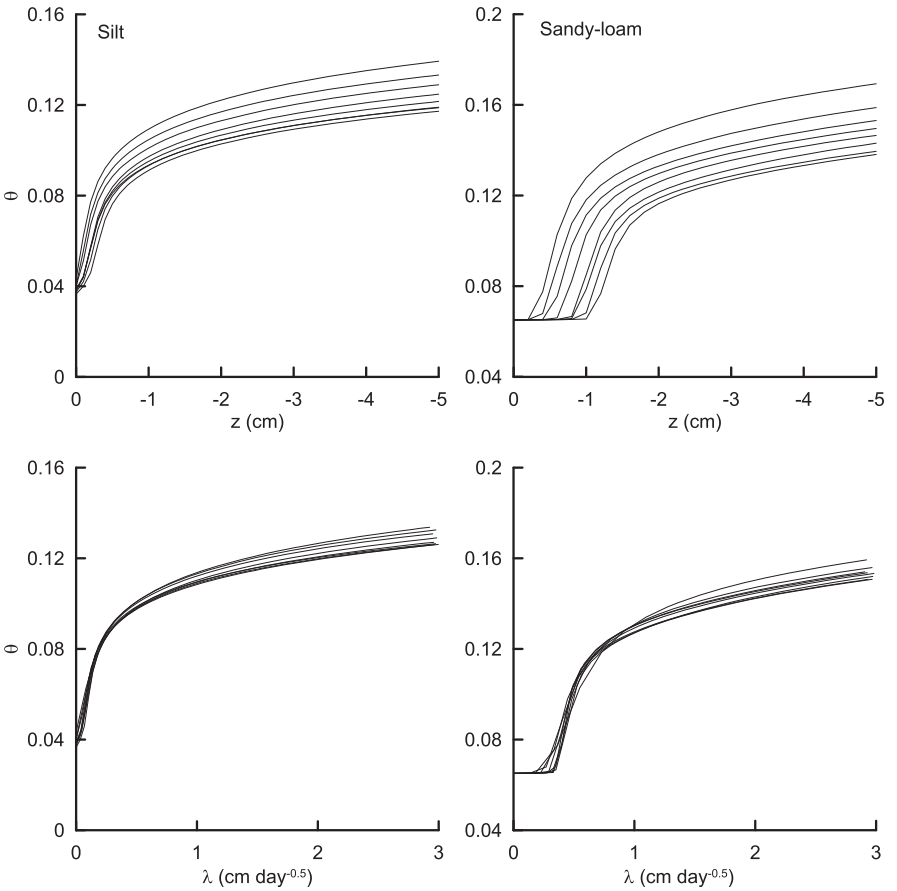

Figure 13. Simulated soil moisture profiles at different times in the (left) silty soil and (right) sandy loam soil plotted versus (top plots) depth and versus (bottom plots) the scaled depth $\lambda = |z|\ t^{-0.5}$.

that vapor transport will gain importance under more arid and warmer conditions. Initially drier soil conditions (smaller ψ_i) and higher soil temperatures (higher $K_{v,\psi}$, see Figure 1) will increase the contribution of vapor transport to S_{evap}. But, the effect of temperature gradients that are expected to increase under drier conditions may deteriorate the correlation between S_{evap} and E_{cum}.

The Boltzmann transform of the diffusion equation can also be used to link the shape of the soil moisture profiles to the shape of $D_w(\theta)$. Only when $\frac{dD_w}{d\theta} < 0$, that is, when D_w increases with decreasing θ, a "hooked" $\theta(\lambda)$ or $\theta(z)$ profile can be obtained, that is, $\frac{d^2\theta}{d\lambda^2} > 0$ [*van Keulen and Hillel*, 1974]. Since the

Table 3. Initial, ψ_i, and Surface Pressure Head, ψ_{sur}, and Desorptivity S_{evap} Calculated From Equation (8) With $K_{v\psi} = 0$, and for Two Different Critical Threshold Pressure Heads, $\psi_{sur} = \psi_{crit}$, and S_{evap} Fitted to the Simulated Cumulative Evaporation Using Equation (7) for the Two Different Soils

	cm		cm $d^{-0.5}$				
Texture	ψ_i	ψ_{sur}	S_{evap}	S_{evap} ($K_{v\psi} = 0$)	S_{evap} ($\psi_{sur} = -10^5$ cm)	S_{evap} ($\psi_{sur} = -10^4$ cm)	S_{evap} Fit
Silt	$-2.3\ 10^3$	$-2.6\ 10^6$	0.84	0.83	0.82	0.72	0.83
					E_{cum} stage II (cm)[a]		
			1.82		*1.86*	*1.57*	
Sandy Loam	$-5.0\ 10^1$	$-3.6\ 10^6$	0.39	0.36	0.36	0.36	0.30
					E_{cum} stage II (cm)[a]		
			0.77		*0.73*	*0.73*	

[a]The cumulative evaporation amounts during stage II, E_{cum}, that are simulated by the nonisothermal vapor-water flow model and by the Richards model for two different ψ_{crit}s are given in italics for the corresponding S_{evap} values.

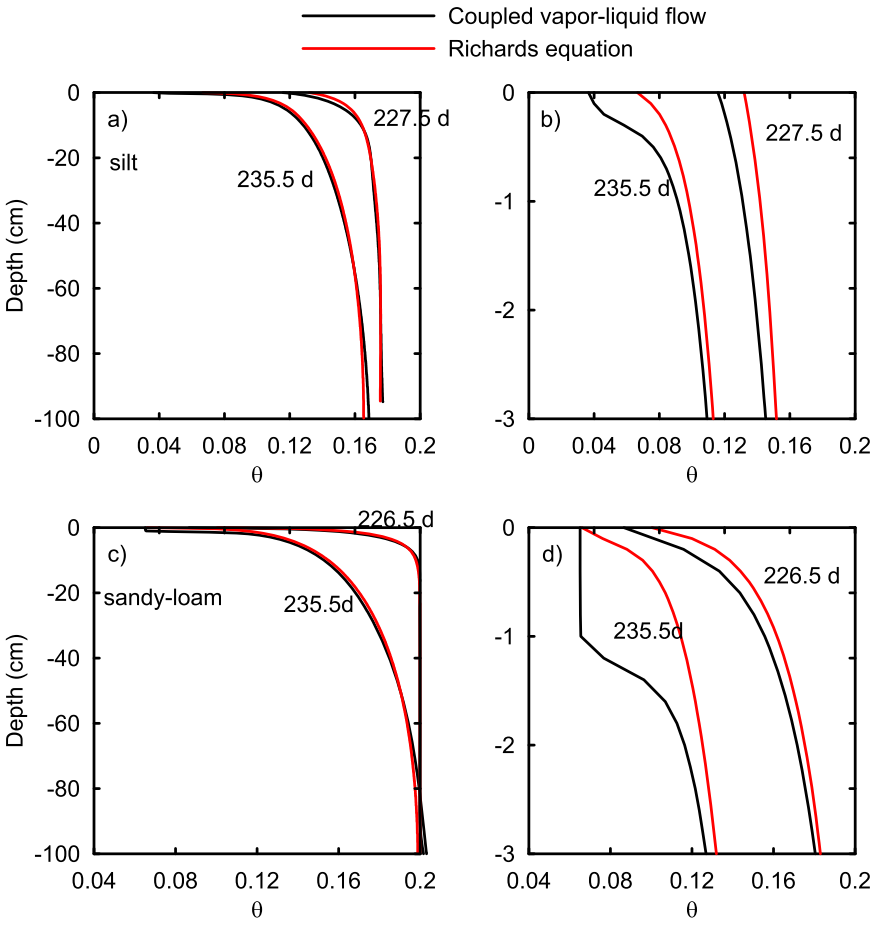

Figure 14. Depth profiles of the water content simulated using a nonisothermal vapor-water flow model (black line) and the Richards equation (red line) in the (top plots) silt and (bottom plots) sandy loam soil. The right plots zoom in the top 3 cm of the soil profile.

effective vapor diffusion coefficient increases with increasing volumetric air content, that is, when θ decreases, considering vapor flow leads to $\frac{dD_w}{d\theta} < 0$ for small volumetric water content and therefore explains the S-shaped or hooked water content profiles close to the soil surface (Figure 13). When only $K_{l,\psi}$ is considered in D_w, $\frac{dD_w}{d\theta} > 0$, so that the Richards model cannot reproduce hooked $\theta(z)$ profiles (Figure 14). Although the differences in simulated water content profiles close to the soil surface between the nonisothermal vapor water flow model and the Richards model did not have a large impact on the simulated soil water balance, these differences might have important impacts on the interpretation of surface soil moisture contents that are observed by remote sensing [*Moghadas et al.*, 2013]. Monitoring the change of the shape of the soil moisture profile close to the soil surface may be used to determine the time when evaporation shifts from stage I to stage II evaporation. Besides active off-ground radar systems, also portable NMR (nuclear magnetic resonance) systems bear potential to obtain vertical soil moisture profiles with high spatial resolution and can be used determine the shift of the evaporation process from stage I to stage II [*Merz et al.*, 2014, 2015].

4.5. Profiles of Liquid and Vapor Fluxes, Liquid Water Content, and Soil Temperature

Figure 15 shows depth profiles of total water fluxes, liquid water fluxes, and vapor fluxes during midday at DOY 235.5 that were simulated by the nonisothermal vapor-water flow model. Deeper in the soil profile, the total water flux is dominated by liquid flow whereas close to the soil surface, liquid water flow goes to zero and upward (positive) water vapor flow dominates. The depth at which the upward liquid flow starts gradually decreasing and the vapor flux increasing with height indicates the evaporative front within the soil profile. This evaporation front is not a sharp interface but a transition zone where evaporation in the subsurface takes place, which is also confirmed by experimental observations [*Heitman et al.*, 2008a, 2008b].

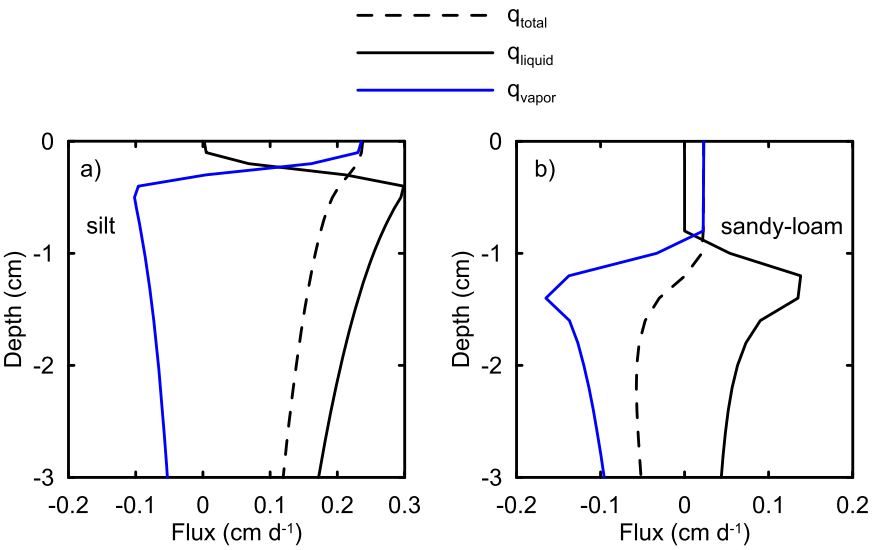

Figure 15. Depth profiles of the total water flux (q_{total}, dashed black line), the liquid water flux (q_{liquid}, solid black line), and the vapor flux (blue line q_{vapor}) in the (left) silt soil and in the (right) sandy loam soil at DOY 235.5. The water fluxes are given in equivalent depths of liquid water.

After 10 days of evaporation, the evaporative front in both soils was still quite close to the soil surface, at 2–3 mm below the surface in the silt soil and at 1 cm below the surface in the sandy loam soil. In both soils, the upward liquid flow toward the evaporating front was larger than the evaporation rate at the soil surface. Part of the evaporating water is transported back into the deeper soil by vapor flow, which is negative and downward below the evaporating surface. The evaporation front corresponds with the bend in the soil moisture profiles close to the soil surface that are simulated by the nonisothermal vapor liquid flow model.

The evaporation front below the soil surface also left an imprint on the soil temperature profile with a larger temperature gradient above than below the evaporation front, which functions as a sink term for heat flow (Figure 16). This sink term, which can be derived from measured temperature profiles with a high vertical resolution combined with estimates of soil thermal properties may be used to estimate the soil evaporation rate [e.g., *Heitman et al*., 2008a, 2008b; *Sakai et al*., 2011].

Soil surface or skin temperatures are closely linked to soil evaporation, which depends during stage II, in part, on soil hydraulic properties. Figure 17 shows simulated soil surface temperatures of the drying silt and

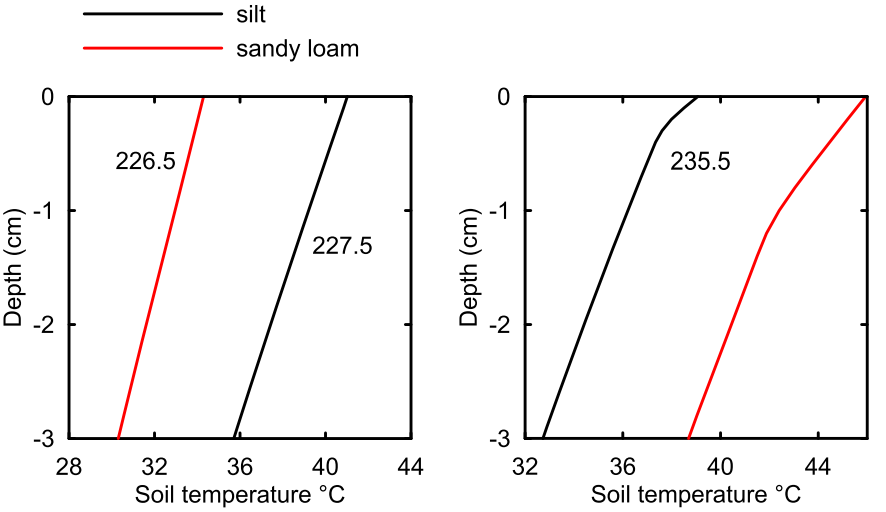

Figure 16. Depth profiles of soil temperature at the (left) beginning and (right) end of the simulation period in the silt (black line) and sandy loam soil (red line).

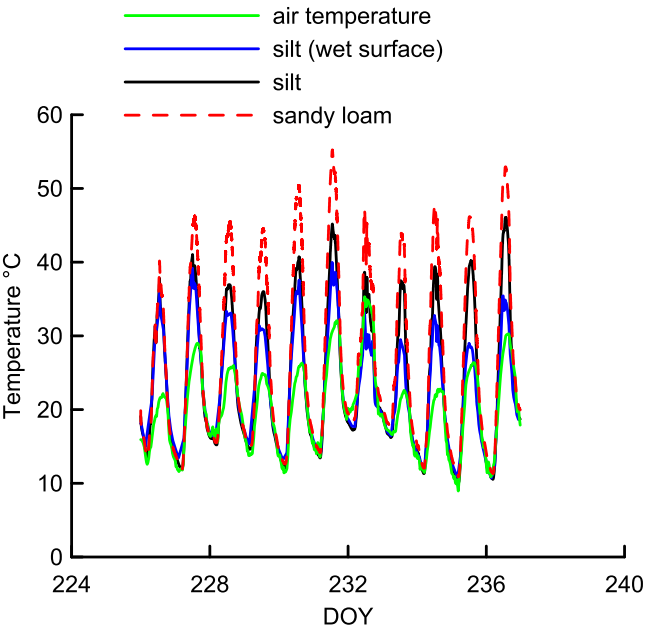

Figure 17. Air temperature (green line) and simulated surface temperature of a silt soil (black), a sandy loam (dashed red), and a silt soil with a wet surface (blue).

sandy loam soils, of a wet silt soil surface, and of the air temperature, which was used as a boundary condition. When the evaporation rate started deviating from the potential evaporation, that is, after about 0.5 days in the sandy loam and 1.5 days in the silt soil (Figure 10), the soil surface temperature of the drying soils became higher than that of a wet soil surface. The time for the onset of the transition from stage I to stage II evaporation, as well as the degree with which the evaporation rate and consequently the soil surface temperature deviate from the wet soil surface, differed between the two different soils. Soil surface temperatures of the sandy loam soil started increasing faster and to a larger extent than those of the silt soil. The different hydraulic behavior of the two soils led to differences in soil surface temperature of up to 10°C. Monitoring soil surface temperature may therefore be used to identify soil hydraulic properties [e.g. *Chanzy et al*., 1995; *Steenpass et al*., 2010] or to identify when evaporation shifts from stage I to stage II [*Tolk et al*., 2015].

It should be noted though that the hydraulic properties of the soil surface layer may differ considerably from those of the subsoil due to soil tillage [*Steenpass et al*., 2010]. Soil tillage may also affect the roughness of the soil surface and therefore momentum, sensible and latent heat transfer between the soil surface and the air flow, but also albedo and net radiation. Since the aerodynamic resistance for mass and heat transfer in the free air flow decreases with increasing surface roughness (see Figure 2 P1), the surface temperature of a rough evaporating surface is lower than that of a smooth surface. For the silt soil, the difference is up to 2°C (Figure 18), which was rather small compared with the difference in surface temperature between the two soils due to differences in evaporation resulting from differences in hydraulic soil properties. A similar conclusion was drawn by *Dimitrov et al*. [2015] who compared surface temperatures of plots with different surface roughness and found only small temperature differences during stage I evaporation.

4.6. Sensitivity of Simulated Evaporation on the Parameterization of Vapor Transport

In the previous examples, vapor transport in the soil was assumed to occur only due to diffusion. An enhancement factor η was used to account for an increase in vapor transport due to a thermal gradient, which may be larger in the air phase than in the bulk soil due to local thermal nonequilibria. In order to investigate the relevance of the enhancement factor and turbulent diffusivity within the porous medium on simulated evaporation fluxes, we considered four cases: (i) reference with an enhancement factor η, (ii) no enhancement factor, (iii) an enhancement factor together with an augmented diffusion coefficient by a factor 10 to represent turbulent diffusion, and (iv) no enhancement factor, but an augmented diffusion coefficient by a factor 10 to represent turbulent diffusion.

In Figure 19, the simulated evaporation fluxes for the different cases in the sandy loam soil are shown and in Figure 20, depth profiles of the simulated liquid and isothermal and thermal vapor fluxes at DOY 235.5. Around midday, a strong positive temperature gradient existed at the soil surface, which led to a downward thermal vapor flux. This downward thermal vapor flux was enhanced by the enhancement factor and compensated the upward isothermal vapor flux from the wetter subsoil toward the dry soil surface (Figure 20). The enhancement factor therefore tended to reduce the net vapor fluxes during the day when radiation is the highest. For the case with an enhancement factor and a diffusion coefficient that is a factor 10 higher, the thermal vapor fluxes compensated the isothermal vapor fluxes completely. In this case, the highest evaporation fluxes were simulated during the morning and evening when the thermal gradients near the

soil surface were small (Figure 19). Whether this simulated temporal evolution of the evaporation rate is realistic is questionable. When no enhancement factor was used, the vapor flux followed more closely the diurnal radiation dynamics and cumulative vapor losses were larger. Based on daily evaporation losses, it is difficult to discriminate the effect of enhanced vapor transport from the effect of soil hydraulic properties. Monitoring the dynamics of bare soil evaporation, for example, using eddy covariance measurements, Bowen ratios or high precision lysimetry, seems to be promising to elucidate the impact or relevance of enhancement factors for vapor transport. Data of hourly evaporation rates measured in lysimeters [e.g., *Novak*, 2010; *Tolk et al*., 2015; *Van Bavel and Reginato*, 1965; *Yang et al*., 2014] or at higher temporal resolutions measured with eddy covariance indicate that also during stage II, evaporation rates follow the diurnal dynamics of the radiation, which indicates that enhancement factors for nonisothermal vapor transport may be less important.

4.7. Parameterization of Transfer Resistances for a Semicoupling of the Richards Equation With Evaporative Forcing

The semicoupled approach should be able to reproduce diurnal evaporation dynamics. To evaluate this approach, we derived β factors (ratio of the aerodynamic resistance to the sum of the soil surface and aerodynamic resistance) from evaporation rates and soil moisture contents of the top layer at midday that were simulated using the coupled nonisothermal vapor-water flow model (Figure 21). A problem with the semicoupled approach is that the thickness of the soil surface layer is not defined. Therefore, we calculated average moisture contents in surface layers of 0.4, 1, and 2 cm thickness and plotted the β factors versus these averaged water contents.

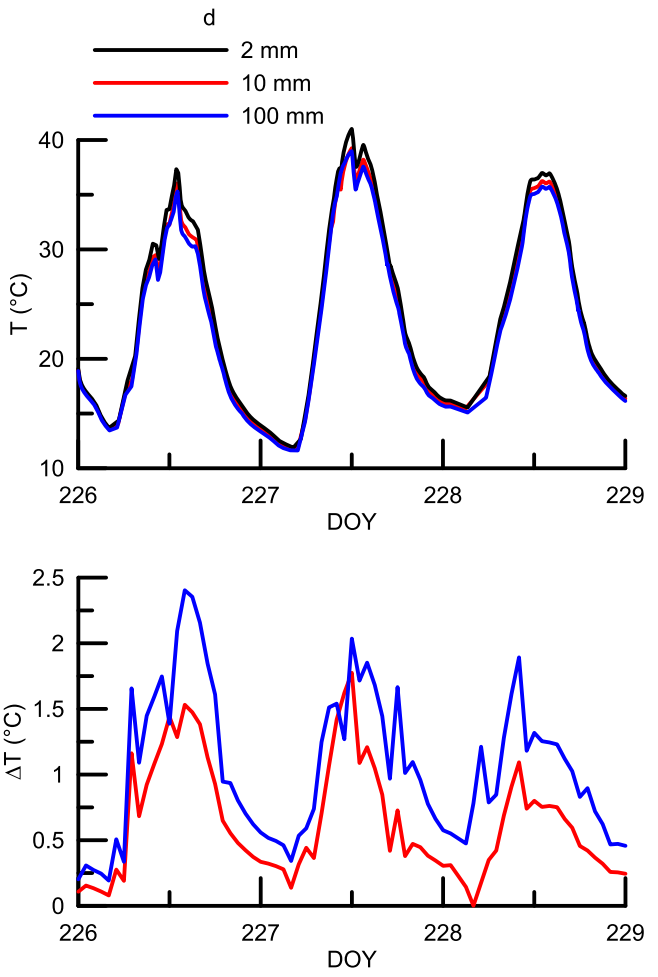

Figure 18. Effect of surface roughness length, d, on simulated soil surface temperature of the silt soil. (top) Surface temperatures over a 3 day period for d = 2, 10, and 100 mm. (bottom) The temperature difference between the surface with a 2 mm roughness and the other two surfaces.

The simulation results indicated a strong dependence of the β factor on the chosen thickness of the soil surface layer. When the soil surface layer is thin and the evaporation front sinks below the bottom of the surface layer, the β factor becomes independent of the water content in the surface layer. Another problem with this approach is that the effect of temperature and temperature gradients on the soil surface resistance term is not considered. We calculated β factors from simulations using the reference enhancement factor, η, and simulations that do not use an enhancement factor. For the latter simulations, the impact of downward thermal gradients on the evaporation flux was much smaller so that for the same water content in the surface layer, a higher evaporation flux (higher β) was obtained. Difference in β factors obtained from these simulations demonstrates the sensitivity of the β factors to not well-characterized processes such as enhancement of fluxes due to temperature gradients. Finally, the scatter of the relation between β and θ for a certain enhancement factor and layer thickness could be related to the differences in temperature in the surface layer with

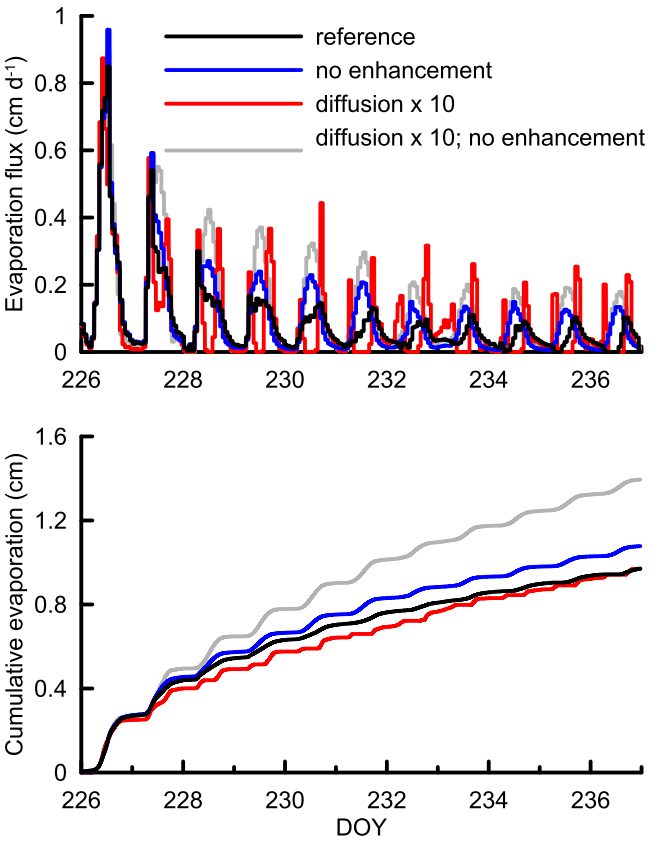

Figure 19. Effect of enhancement factor and vapor diffusion on (top) simulated evaporation and (bottom) cumulative evaporation from the sandy loam soil using the reference parameterization (black line), an enhancement factor $\eta = 1$ for $K_{v,T}$, no-enhancement, blue line), a higher diffusion coefficient for vapor transport in the air phase to account for turbulent pumping (diffusion x 10, red line), a higher diffusion coefficient for vapor transport and an enhancement factor $\eta = 1$ (diffusion x 10, no enhancement, grey line).

higher temperatures leading to a positive deviation and lower temperatures to a negative deviation.

5. Conclusions

Lateral variations in soil properties, water infiltration, and/or radiation lead to lateral variations in state variables and fluxes. At the soil surface, these variations are coupled to transfer processes in the free flow and the soil. When the soil surface is sufficiently wet, the evaporation does not depend on the local hydraulic properties of the soil and their spatial variability. The evaporation rate from wet surfaces can be assumed to be nearly uniform and to vary little in the main wind direction for sufficiently large and uniform areas with a sufficiently large fetch. This uniform evaporation rate could be calculated using vertical gradients of air temperature, air humidity, and wind speed in the free flow, net radiation on the porous medium surface and a surface energy balance.

The potential evaporation could be used as a uniform boundary condition for a 3-D flow model in a heterogeneous wet porous medium and could serve as boundary condition for upscaling heterogeneous flow in the vadose

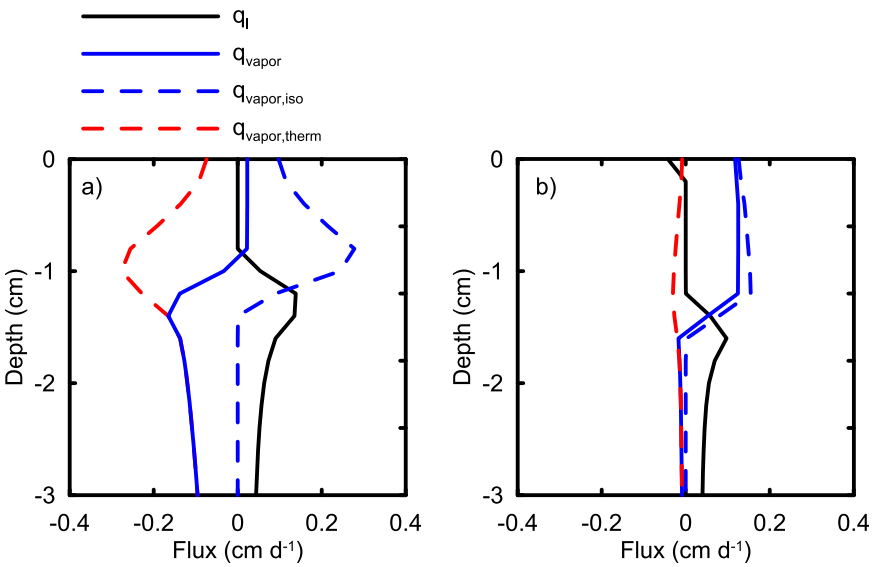

Figure 20. Effect of enhancement factor and vapor diffusion on depth profiles of liquid water fluxes and isothermal and thermal vapor fluxes: (a) reference case and (b) no enhancement factor.

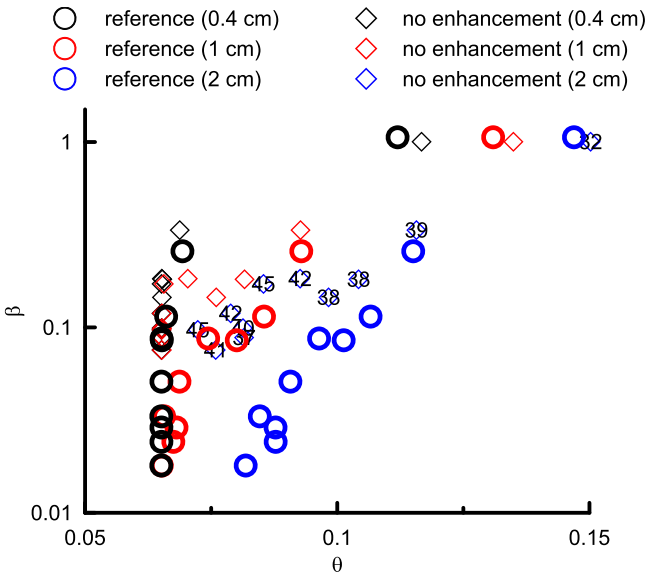

Figure 21. β factor that expresses the reduction of the soil evaporation as compared to the evaporation of a wet surface as a function of the water content of a top soil layer. Different colors refer to different thickness of the top soil layer and different symbols refer to simulations considering an enhancement of vapor fluxes due to a thermal gradient (circles) and simulations that do not consider this enhancement (diamonds). Labels in the blue diamond symbols refer to the average temperature in the surface layer.

zone [*Li et al.*, 2015]. However, problems arise when parts of the heterogeneous surface dry out so that the evaporation flux from these parts decreases. A commonly used approach to simulate such cases is to use a threshold boundary condition as used in 1-D models [*Schlüter et al.*, 2012] or to use 1-D aerodynamic transfer resistances that depend on the soil water content. However, such approaches do not account for an increase in evaporation from wet parts of the heterogeneous surface that arise from lateral variations in free flow variables (air humidity and air temperature) due to variations in evaporation and evaporative cooling on the soil surface [*Bechtold et al.*, 2012]. Also, lateral heat fluxes within the soil can contribute to an enhanced evaporation from wet soil patches [*Shahraeeni and Or*, 2011]. Our simulation studies demonstrated that lateral heat fluxes in the soil play an important role and neglecting them leads to an underestimation of the evaporation rate from wet patches. It should be noted that in our simulations, we did not consider radiation. We expect that radiation will increase the importance of lateral heat fluxes.

Models that couple free flow with processes in the porous medium can be used to simulate compensatory evaporation from wet patches on a heterogeneous surface. However, such simulations are computationally expensive. Therefore, correction factors, which depend on free flow conditions, porous medium properties, and the spatial scale and geometry of wet patches, to adjust evaporation from wet patches that can be used as boundary conditions in porous media models could be of practical importance. It should be noted that such correction factors have already been derived to estimate, for instance, the effect of the size of evaporation pans, ponds, or lakes on the evaporation from these surfaces. However, these factors do not account for lateral heat and water flow within the porous medium.

For large fetches, when lateral variations in state variables and vertical fluxes in the free flow and the porous medium can be neglected, one-dimensional modeling approaches can be used. The main differences between these models are the description of vapor fluxes in the porous medium and the coupling between heat and water balances. The Richards equation, which neglects vapor fluxes and which is not coupled to a heat flow equation in the porous medium, simulated similar cumulative evaporation as the more comprehensive model that includes vapor transport in the porous medium. The effect of neglecting vapor transport in the porous medium and the choice of the threshold boundary pressure head, ψ_{crit}, on simulated cumulative evaporation fluxes could be evaluated using the desorptivity, which is an integral function of the hydraulic conductivity. When vapor transport in the porous medium was more important than liquid flow, the diurnal dynamics of evaporation could not be reproduced by the Richards equation using a threshold boundary condition, which decouples evaporation dynamics from the dynamics of evaporative forcing during stage II evaporation. However, a boundary condition for the Richards equation that combines the diurnal dynamics of the evaporation of a wet surface (evaporative forcing) with a soil surface resistance depending on the soil water content could be used to reproduce the diurnal evaporation dynamics. In this so-called semicoupled approach, which is often used in large scale simulation models, the heat fluxes in the porous medium are not considered and heat and water balances are only coupled at the porous medium free flow interface. The parameterization of this soil resistance term depends on the thickness of the considered soil surface layer and on the effect of temperature and

temperature gradients on evaporation. The latter indicates that this resistance term should depend on the climatic conditions.

Vapor transport and its parameterization representing processes like turbulent pumping and thermal nonequilibrium mainly affect the diurnal dynamics of evaporation. Monitoring the diurnal dynamics of evaporation therefore provides indirect information about processes controlling vapor transport in porous media and could be useful to parameterize nonequilibria processes.

Neglecting vapor transport in the Richards equation and decoupling heat and water fluxes in the porous medium also has an impact on the predicted soil moisture and temperature profiles close to the soil surface. Due to the monotonous increase of the water diffusivity with increasing water content when vapor transport is not considered, Richards' equation cannot predict "hooked" water content profiles that develop when the evaporation front recedes within the porous medium. Since vapor transport in the porous medium is not considered, the Richards equation assumes that the evaporation takes places at the soil surface. Therefore, it cannot simulate the development of an evaporation front that recedes in the porous medium neither the effect of this front on the temperature profile nor the surface temperature. Derivation of evaporation rates from remotely sensed surface temperature data or detailed measurements of temperature profiles therefore requires models that couple heat, water, and vapor transport in the soil.

Acknowledgments
The authors would like to acknowledge the German Science Foundation, DFG. This work is a contribution of the DFG research unit "Multi-Scale Interfaces in Unsaturated Soil" (MUSIS; FOR 1083) and the DFG International Research Training Group NUPUS and the National Science Foundation (NSF EAR-1447533). The modified Hydrus source code and the input files necessary to reproduce the simulations are available from the authors upon request. The DuMu^x source code and its input files are available via https://git.iws.uni-stuttgart.de/dumux-pub/Fetzer2017b. The authors would like to thank the editor and the anonymous reviewers for their insightful comments and suggestions that have contributed to improve this paper.

References

Assouline, S., S. W. Tyler, J. S. Selker, I. Lunati, C. W. Higgins, and M. B. Parlange (2013), Evaporation from a shallow water table: Diurnal dynamics of water and heat at the surface of drying sand, *Water Resour. Res.*, *49*, 4022–4034, doi:10.1002/wrcr.20293.

Baber, K., K. Mosthaf, B. Flemisch, R. Helmig, S. Müthing, and B. Wohlmuth (2012), Numerical scheme for coupling two-phase compositional porous-media flow and one-phase compositional free flow, *IMA J. Appl. Math.*, *77* (6), 887–909, doi:10.1093/imamat/hxs048.

Bastian, P., M. Blatt, A. Dedner, C. Engwer, R. Klöfkorn, M. Ohlberger, and O. Sander (2008a), A generic grid interface for parallel and adaptive scientific computing. Part i: Abstract framework, *Computing*, *82*(2–3), 103–119, doi:10.1007/s00607-008-0003-x.

Bastian, P., M. Blatt, A. Dedner, C. Engwer, R. Klöfkorn, R. Kornhuber, M. Ohlberger, and O. Sander (2008b), A generic grid interface for parallel and adaptive scientific computing. Part ii: Implementation and tests in dune, *Computing*, *82* (2–3), 121–138, doi:10.1007/s00607-008-0004-9.

Bechtold, M., J. Vanderborght, L. Weihermuller, M. Herbst, T. Gunther, O. Ippisch, R. Kasteel, and H. Vereecken (2012), Upward transport in a three-dimensional heterogeneous laboratory soil under evaporation conditions, *Vadose Zone J.*, *11*(2), 21, doi:10.2136/vzj2011.0066.

Black, T. A., W. R. Gardner, and G. W. Thurtell (1969), Prediction of evaporation, drainage, and soil water storage for a bare soil, *Soil Sci. Soc. Am. Proc.*, *33*(5), 655–660.

Boesten, J. J. T. I., and L. Stroosnijder (1986), Simple-model for daily evaporation from fallow tilled soil under spring conditions in a temperate climate, *Neth. J. Agric. Sci.*, *34*(1), 75–90.

Chanzy, A., L. Bruckler, and A. Perrier (1995), Soil evaporation monitoring: A possible synergism of microwave and infrared remote-sensing, *J. Hydrol.*, *165*(1–4), 235–259, doi:10.1016/0022-1694(94)02571-R.

Dimitrov, M., J. Vanderborght, K. G. Kostov, B. Debecker, P. S. Lammers, L. Damerow, and H. Vereecken (2015), Soil hydraulic parameters of bare soil plots with different soil structure inversely derived from l-band brightness temperatures, *Vadose Zone J.*, *14*(8), 23, doi:10.2136/vzj2014.09.0133.

Flemisch, B., et al. (2011), Dumux: Dune for multi-{phase, component, scale, physics, . . .} flow and transport in porous media, *Adv. Water Resour.*, *34*(9), 1102–1112, doi: 10.1016/j.advwatres.2011.03.007.

Heitman, J. L., R. Horton, T. J. Sauer, and T. M. Desutter (2008a), Sensible heat observations reveal soil-water evaporation dynamics, *J. Hydrometeorol.*, *9*(1), 165–171, doi:10.1175/2007jhm963.1.

Heitman, J. L., X. Xiao, R. Horton, and T. J. Sauer (2008b), Sensible heat measurements indicating depth and magnitude of subsurface soil water evaporation, *Water Resour. Res.*, *44*, W00D05, doi:10.1029/2008WR006961.

Helmig, R., and R. Huber (1998), Comparison of Galerkin-type discretization techniques for two-phase flow in heterogeneous porous media, *Adv. Water Resour.*, *21*(8), 697–711, doi:10.1016/s0309-1708(97)00023-7.

Lehmann, P., and D. Or (2009), Evaporation and capillary coupling across vertical textural contrasts in porous media, *Phys. Rev. E*, *80*(4), 046318, doi:10.1103/PhysRevE.80.046318.

Li, N., L. Ren, and X. Yue (2015), Application and validation of an upscaling method for unsaturated water flow processes in heterogeneous soils, *Vadose Zone J.*, *14*(7), 11, doi: 10.2136/vzj2014.12.0171.

Merz, S., A. Pohlmeier, J. Vanderborght, D. van Dusschoten, and H. Vereecken (2014), Moisture profiles of the upper soil layer during evaporation monitored by NMR, *Water Resour. Res.*, *50*, 5184–5195, doi:10.1002/2013WR014809.

Merz, S., A. Pohlmeier, J. Vanderborght, D. van Dusschoten, and H. Vereecken (2015), Transition of stage i to stage ii evaporation regime in the topmost soil: High-resolution NMR imaging, profiling and numerical simulation, *Microporous Mesoporous Mater.*, *205*, 3–6, doi: 10.1016/j.micromeso.2014.10.035.

Millington, R., and J. P. Quirk (1961), Permeability of porous solids, *Trans. Faraday Soc.*, *57*(8), 1200–1207, doi:10.1039/TF9615701200.

Milly, P. C. D. (1984), A simulation analysis of thermal effects on evaporation from soil, *Water Resour. Res.*, *20*(8), 1087–1098, doi:10.1029/WR020i008p01087.

Moghadas, D., K. Z. Jadoon, J. Vanderborght, S. Lambot, and H. Vereecken (2013), Effects of near surface soil moisture profiles during evaporation on far-field ground-penetrating radar data: A numerical study, *Vadose Zone J.*, *12*(2), 11, doi:10.2136/vzj2012.0138.

Novak, M. D. (2010), Dynamics of the near-surface evaporation zone and corresponding effects on the surface energy balance of a drying bare soil, *Agric. For. Meteorol.*, *150*(10), 1358–1365, doi:10.1016/j.agrformet.2010.06.005.

Parlange, J. Y., M. Vauclin, R. Haverkamp, and I. Lisle (1985), The relation between desorptivity and soil-water diffusivity, *Soil Sci.*, *139*(5), 458–461, doi: 10.1097/00010694-198505000-00012.

Ritchie, J. T. (1972), Model for predicting evaporation from a row crop with incomplete cover, *Water Resour. Res.*, *8*(5), 1204–1213, doi:10.1029/WR008i005p01204.

Saito, H., J. Simunek, and B. P. Mohanty (2006), Numerical analysis of coupled water, vapor, and heat transport in the vadose zone, *Vadose Zone J.*, *5*(2), 784–800, doi:10.2136/vzj2006.0007.

Sakai, M., S. B. Jones, and M. Tuller (2011), Numerical evaluation of subsurface soil water evaporation derived from sensible heat balance, *Water Resour. Res.*, *47*, W02547, doi:10.1029/2010WR009866.

Schlüter, S., H.-J. Vogel, O. Ippisch, P. Bastian, K. Roth, H. Schelle, W. Durner, R. Kasteel, and J. Vanderborght (2012), Virtual soils: Assessment of the effects of soil structure on the hydraulic behavior of cultivated soils, *Vadose Zone J.*, *11*(4), 15, doi:10.2136/vzj2011.0174.

Shahraeeni, E., and D. Or (2011), Thermo-evaporative fluxes from heterogeneous porous surfaces resolved by infrared thermography, *Water Resour. Res.*, *46*, W09511, doi:10.1029/2009WR008455.

Simunek, J., M. Sejna, H. Saito, M. Sakai, and M. T. van Genuchten (2008), *The hydrus-1d software package for simulating the movement of water, heat, and multiple solutes in variably saturated media*, version 4.08, report, 330 pp., Dep. of Environ. Sci., Univ. of Calif. Riverside, Riverside.

Šimůnek, J., M. T. van Genuchten, and M. Šejna (2016), Recent developments and applications of the hydrus computer software packages, *Vadose Zone J.*, *15*(7), 25, doi:10.2136/vzj2016.04.0033.

Steenpass, C., J. Vanderborght, M. Herbst, J. Simunek, and H. Vereecken (2010), Estimating soil hydraulic properties from infrared measurements of soil surface temperatures and TDR data, *Vadose Zone J.*, *9*(4), 910–924, doi:10.2136/vzj2009.0176.

Tolk, J. A., S. R. Evett, and R. C. Schwartz (2015), Field-measured, hourly soil water evaporation stages in relation to reference evapotranspiration rate and soil to air temperature ratio, *Vadose Zone J.*, *14*(7), 14, doi:10.2136/vzj2014.07.0079.

Van Bavel, C. H. M., and R. J. Reginato (1965), *Precision Lysimetry for Direct Measurement of Evaporative Flux*, 129–135 pp., U. N. Educ., Sci., and Cult. Organ., Paris.

van Genuchten, M. T. (1980), A closed-form equation for predicting the hydraulic conductivity of unsaturated soils, *Soil Sci. Soc. Am. J.*, *44*(5), 892–898, doi:10.2136/sssaj1980.03615995004400050002x.

van Keulen, H., and D. Hillel (1974), Simulation study of drying-front phenomenon, *Soil Sci.*, *118*(4), 270–273.

Weishaupt, K., et al. (2016), DuMuX 2.9.0, Zenodo, Switzerland. [Available at http://doi.org/10.5281/zenodo.48256.]

Yang, G. J., R. L. Pu, C. J. Zhao, and X. Z. Xue (2014), Estimating high spatiotemporal resolution evapotranspiration over a winter wheat field using an ikonos image based complementary relationship and lysimeter observations, *Agric. Water Manage.*, *133*, 34–43, doi:10.1016/j.agwat.2013.10.018.